Effects of thrust, tip-speed ratio, and time variations on wind-turbine wakes at high Reynolds numbers

Nathaniel J. Wei[1,2]†**, Adina Y. Fleisher**[3]**, John W. Kurelek**[4]**, and Marcus N. Hultmark**[3]

[1]Mechanical Engineering and Applied Mechanics, University of Pennsylvania, Philadelphia, PA 19104, USA

[2]Andlinger Center for Energy and the Environment, Princeton University, Princeton, NJ 08544, USA

[3]Mechanical and Aerospace Engineering, Princeton University, Princeton, NJ 08544, USA

[4]Mechanical and Materials Engineering, Queen's University, Kingston, ON, Canada K7L 3N6

The evolution of rotor wakes is an important problem for a wide range of wind-energy and aerodynamic applications, and is of particular relevance to dynamic wake control strategies for wind farms. This study aims to clarify the influence of turbine thrust and tip-speed ratio on tip-vortex breakdown and the evolution of the near wake. Scaling arguments show that these parameters contribute to the wake dynamics in distinct ways, and that neither thrust nor tip-speed ratio are alone sufficient to describe near and intermediate wake development. These considerations are especially critical for time-varying flows. To demonstrate these principles, a wind turbine at a near utility-scale Reynolds number ($Re_D = 4 \times 10^6$) is forced in periodic rotation-rate oscillations at low Strouhal numbers ($St = 0.04$). The slow time-varying forcing protocol decouples thrust and tip-speed ratio effects without introducing nonlinear dynamics into the wake that would appear at higher forcing frequencies. Flow measurements in the wake of the turbine show disturbances propagate through the wake as traveling waves, with thrust and tip-speed ratio variations displaying synergistic or competing effects on wake dynamics depending on the relative phase and amplitude of such disturbances. The results provide key insights into the dynamics of time-varying wakes, limitations in existing models of rotor wake dynamics, and to future novel wake-control schemes.

Key words: Aerodynamics, vortex dynamics, wakes

1. Introduction

The rapid expansion of wind energy is a critical task for the global transition towards a more environmentally sustainable energy economy. A major challenge facing large-scale wind energy development is the downstream impacts of wind-turbine and wind-farm wakes. In large wind farms, power-generation losses due to wakes from upstream turbines are often on

† Email address for correspondence: njwei@seas.upenn.edu

the order of 10 to 20% (Barthelmie *et al.* 2009), with individual turbine losses approaching 40 to 50% in some cases (Barthelmie *et al.* 2010; Howland *et al.* 2019). As wind farms grow larger and more prevalent worldwide, these wake losses represent stark inefficiencies that, if reduced, could result in significant improvements in power generation and reductions in the levelized cost of energy for wind farms. Wind-turbine wake dynamics are therefore of immense importance for humanity's efforts to mitigate the long-term effects of anthropogenic climate change.

Appropriately, a large body of research on wind-turbine wake dynamics exists in the literature (cf. Stevens & Meneveau 2017; Porté-Agel *et al.* 2020). In this study, we focus on the recovery of the wake, which directly affects wake losses incurred by downstream turbines and the overall power density of a wind-turbine array. According to one-dimensional (1D) momentum theory, the velocity deficit in the wake of a turbine is a function of the thrust coefficient, defined as

$$C_t = \frac{F_x}{\frac{1}{2}\rho U_\infty^2 A},\tag{1.1}$$

where F_x is the streamwise force on the turbine rotor, ρ is the fluid density, U_∞ is the free-stream velocity, $A = \frac{\pi}{4}D^2$ is the swept area of the turbine, and D is the turbine diameter. Conservation relations dictate that, at least for relatively low axial induction factors, a higher thrust coefficient leads to a stronger wake-velocity deficit. The 1D momentum-theory model breaks down under high thrust-loading conditions, and a number of methods have recently been developed to correct for these inaccuracies (Steiros & Hultmark 2018; Bempedelis & Steiros 2022; Liew *et al.* 2024). These approaches extend the conclusion that higher thrust produces a stronger wake to arbitrary loading conditions.

A typical axisymmetric turbulent wake will recover from this initial velocity deficit as the flow evolves downstream, driven by the turbulent entrainment of momentum from the undisturbed free stream surrounding the wake (Uberoi & Freymuth 1970). However, unlike the canonical bluff-body case, wind-turbine wakes feature a system of helical tip vortices that plays a key role in defining the near, intermediate, and far wake regions. The helical tip vortices are shed by the rotating turbine blades and form a cylindrical 'shell' that shields the near wake from the free stream (Porté-Agel *et al.* 2020). These vortex elements undergo a mutual-inductance instability in which neighboring vortices pair up and eventually break down (Widnall 1972; Okulov & Sørensen 2007; Sarmast *et al.* 2014; Sørensen *et al.* 2015). These dynamics are dependent on the tip-speed ratio of the turbine, defined as

$$\lambda = \frac{\Omega D}{2U_\infty},\tag{1.2}$$

where Ω is the rotation rate of the turbine. The breakdown of the helical tip vortex (typically around $2 \lesssim x/D \lesssim 4$) marks the transition into the intermediate wake, in which shear layers grow inwards from the wake boundary toward the centerline. The far-wake region begins after the shear layers reach the centerline and all signatures of the near-wake vortex system, and thus properties of the rotor, can no longer be identified (Vermeer *et al.* 2003). In steady flow, it is well-established that the far wake behaves in a self-similar manner (*e.g.*, Bastankhah & Porté-Agel 2014). Characteristics of the tip-vortex system can be related to the turbine thrust coefficient, for instance by Biot-Savart induction (as done in free-vortex wake models, *e.g.*, Segalini & Alfredsson 2013; de Vaal *et al.* 2014) or by impulse theory (Limacher *et al.* 2022). Therefore, a full account of wind-turbine wake recovery must consider both thrust and rotational dynamics.

Common to experimental and numerical investigations of turbine wake dynamics is the

use of simplifying models, either to reduce the complexity of experimental setups or the computational costs of simulations, ultimately leading to aspects of the mechanistic picture presented above being neglected. For example, many numerical studies of wind farms use actuator-disc models (*e.g.*, Calaf *et al.* 2010; Meyers & Meneveau 2012; Goit & Meyers 2015), in which turbines are modeled as porous discs that impart a streamwise thrust force to the flow. This approach notably lacks imparting angular momentum and the helical tip vortex system to the near wake, and therefore can only serve to model far-wake behaviors (Aubrun *et al.* 2013; Lignarolo *et al.* 2014; Kurelek *et al.* 2023). On the other hand, most experimental studies in wind tunnels and water channels are limited in model size and/or maximum flow velocity, thus limiting investigations to Reynolds numbers that are orders of magnitude lower than those of utility-scale wind turbines (*e.g.*, Krogstad & Adaramola 2012; Zhang *et al.* 2012; Bartl *et al.* 2018), and thus rely on Reynolds number invariance arguments that remain to be proven definitively (Chamorro *et al.* 2012; Miller *et al.* 2019). Lastly, most studies of wind turbine wakes assume steady inflow and operating conditions, in stark contrast to the turbulent and continuously evolving nature of winds in the atmospheric boundary layer (Leishman 2002). While the simplifying assumptions laid out above can be appropriate in certain situations, a more comprehensive investigation of near-wake breakdown and subsequent recovery is warranted given the many instances where these assumptions break down.

Of particular relevance is the recent advent of dynamic wake control for wind-farm power optimization, where a number of strategies have emerged seeking to exploit unsteady mechanisms in wind-turbine wakes to accelerate wake recovery and thereby enhance wind-farm power density (cf. Meyers *et al.* 2022). For example, Brown *et al.* (2022) demonstrated intracycle rotation-rate perturbations can alter the spacing between tip vortices, encouraging pairwise interactions and leading to a faster breakdown of the helical tip-vortex structure. In a different approach, known as dynamic induction control, the thrust force of the turbine is perturbed in periodic oscillations (Goit & Meyers 2015; Munters & Meyers 2017, 2018). This can be done by periodically varying the collective pitch angle of the turbine blades (e.g. Frederik *et al.* 2020*b*; van der Hoek *et al.* 2022), varying the individual blade pitch azimuthally to create a nonuniform rotating thrust profile (e.g. Frederik *et al.* 2020*a*; van der Hoek *et al.* 2024), or moving the turbine itself in periodic oscillations, which is a possibility for floating offshore wind turbines (Messmer *et al.* 2024). In these scenarios, steady-flow assumptions cannot be invoked and tip-vortex dynamics play a salient role (Wei *et al.* 2024). Unsteady dynamics may also decouple the turbine thrust from the tip-speed ratio due to the effects of inertia, generator loading, and unsteady blade aerodynamics (El Makdah *et al.* 2021; Wei & Dabiri 2022, 2023). Additionally, dynamic wake control has not currently been tested at utility-scale Reynolds numbers. Thus, these time-varying applications further underscore the need for a careful consideration of the effects of turbine thrust and tip-vortex dynamics on wake evolution and recovery.

The aim of the present study is to clarify the effects of turbine thrust and tip-vortex breakdown on wake recovery at high Reynolds numbers, in a manner that applies in both steady and time-varying contexts. Section 2 outlines scaling arguments for the breakdown of the near wake that employs a more general and thus less restrictive set of assumptions than previous methods in the literature. These hypotheses are then investigated experimentally at utility-scale Reynolds numbers using a horizontal-axis wind turbine operated at a slowly time-varying rotation rate, as described in section 3. Results from these experiments, documented in section 4, highlight differences in the effects of thrust and tip-speed ratio on the near and intermediate wake regions. Additionally, the relatively slow time variations in the turbine forcing show distinct wake behaviors from steady-flow cases, emphasizing the importance of

these time-varying dynamics for wake modeling. Implications of these results for wind-farm modeling and control are discussed in section 5.

2. Theoretical considerations

2.1. *Scaling arguments for tip-vortex breakdown in the near wake*

It is often assumed that turbine thrust is the most significant parameter governing the physics of wake recovery. For the transition from the near to the far wake, however, the evolution and breakdown of the helical tip-vortex system is also important to consider. This process sets the initial conditions for far-wake recovery by turbulent entrainment, and therefore can play a central role in dynamic wake control strategies. Here, we revisit assumptions about these dynamics by means of scaling arguments, which provide insights into time-varying and non-equilibrium wind-turbine wakes.

As outlined in the previous section, the transition between the near- and far-wake regions is governed by the breakdown of the helical tip vortices shed by the turbine blades. This process is dominated by the mutual-inductance instability, though other mechanisms may be active (*e.g.*, Widnall 1972; Cerretelli & Williamson 2003). Higher tip-speed ratios correspond to a closer spacing between individual tip vortices, and since the induced velocity from a point vortex scales inversely with distance, it is often assumed that this leads to an earlier onset of vortex interactions and thus a faster breakdown of the vortex system (Sørensen *et al.* 2015). This has been corroborated experimentally by Felli *et al.* (2011), Lignarolo *et al.* (2015), Biswas & Buxton (2024), and others. Conversely, Piqué *et al.* (2024) recently found that, at utility-scale Reynolds numbers, higher tip-speed ratios corresponded to extended near-wake regions, an effect they linked to decreased levels in turbulence intensity along the wake boundary.

To resolve these conflicting findings on the behavior of tip-vortex breakdown, we build on the analysis of Sørensen *et al.* (2015), who proposed that the streamwise tip-vortex breakdown location, x_b, can be modeled as

$$\frac{x_b}{D} = -\frac{8\,(U_c/U_\infty)^3}{N_B \lambda C_t} \ln\left(c T_i\right), \tag{2.1}$$

where U_c is the convective velocity in the wake, N_B is the number of turbine blades, T_i is the free-stream turbulence intensity, and c is a proportionality constant. Based on the model of Sørensen & Van Kuik (2011) for wind turbines operating at low tip-speed ratios, they argued that

$$C_t \approx \frac{2 N_B \Gamma \lambda}{D U_\infty}, \tag{2.2}$$

where Γ is the total circulation shed from the rotor and is assumed to be entirely contained within the tip vortices. If Γ is assumed to be constant, then $x_b \sim 1/\lambda^2$ and higher tip-speed ratios should correspond to faster tip-vortex breakdown.

However, Γ may not remain constant across different turbine operating conditions. This may be demonstrated by considering the aerodynamic loading on the turbine blades, which simultaneously dictates the torque on the turbine and the circulation of the tip vortices. The Kutta-Joukowsky theorem gives the lift per unit span, F_L/s, on a turbine blade as

$$F_L/s = \rho U_{rel}\Gamma, \tag{2.3}$$

where $U_{rel} = \sqrt{U_\infty^2 + (r\Omega)^2}$ is the apparent inflow velocity at each blade section with

induction effects neglected. Taking the blade length R as the spanwise length scale, the torque on a turbine blade thus scales as

$$\tau_B \sim \rho R^2 \Gamma U_\infty \sqrt{1 + \lambda^2}. \tag{2.4}$$

The power generated by the turbine is then given by

$$\mathcal{P} \sim N_B \tau_B \Omega = N_B \rho R \Gamma U_\infty^2 \lambda \sqrt{1 + \lambda^2}. \tag{2.5}$$

Nondimensionalizing,

$$C_p \equiv \frac{\mathcal{P}}{\frac{1}{2}\rho \pi R^2 U_\infty^3} \sim \frac{2N_B}{\pi R U_\infty} \Gamma \lambda \sqrt{1 + \lambda^2}. \tag{2.6}$$

Since the power curve of a turbine is determined by the aerodynamics of the rotor, Γ is not a free parameter but instead must vary as a function of λ and C_p. To illustrate the implications of this point, consider a hypothetical parabolic power curve of the form

$$C_p = 4C_{p,\max} \frac{\lambda}{\lambda_{\max}} \left(1 - \frac{\lambda}{\lambda_{\max}}\right), \tag{2.7}$$

a concave-down parabola with zeros at $\lambda = 0$ and $\lambda_{\max}$ and a peak of $C_p = C_{p,\max}$ at $\lambda = \lambda_{\max}/2$. Combining equations 2.6 and 2.7, and defining $\lambda^* = \lambda/\lambda_{\max}$, we find

$$\Gamma \sim \frac{\pi D U_\infty C_{p,\max}}{N_B \lambda_{\max}^2} \frac{1 - \lambda^*}{\sqrt{1/\lambda_{\max}^2 + \lambda^{*2}}}, \tag{2.8}$$

which, as shown in figure 1 (blue dashed curve), is a monotonically decreasing function of λ. Applying this relation to equations 2.1 and 2.2 gives the result

$$\frac{x_b}{D} \sim -\frac{8U_c^3 \ln (cT_i)}{\pi D U_\infty^4 C_{p,\max}} \frac{\sqrt{1/\lambda_{\max}^2 + \lambda^{*2}}}{\lambda^{*2} (1 - \lambda^*)}. \tag{2.9}$$

A sample profile of equation 2.9 is shown as a red curve in figure 1, with all parameters held constant except for λ^*. For low tip-speed ratios ($\lambda^* < 1/2$), the tip-vortex breakdown location decreases with increasing λ, in accordance with the typical findings in the literature. However, for tip-speed ratios to the right of $C_{p,max}$, the tip-vortex breakdown location increases with increasing λ. This is a direct result of coupling Γ with λ in accordance with the turbine power curve, rather than assuming it remains constant.

This theoretical demonstration helps clarify the conflicting results reported in prior studies. If Γ is assumed to be constant, then the model of Sørensen & Van Kuik (2011) states that $C_t \sim \lambda$ (equation 2.2). Accordingly, several studies have shown earlier tip-vortex breakdown with increasing λ, including the results of Lignarolo *et al.* (2015) and Biswas & Buxton (2024), where the employed turbine models have characteristic thrust curves that monotonically increase with increasing λ. By contrast, the turbine used by Piqué *et al.* (2024) has a non-monotonic thrust curve that increases with λ at low tip-speed ratios and then decreases with increasing λ for tip-speed ratios above the optimal operating point. As suggested by the preceding analysis, this implies a non-constant Γ for this turbine, and indeed their results show velocity-variance peaks in the near wake that decrease in magnitude when increasing beyond the optimal tip-speed ratio, indicating that tip-vortex circulation is also decreasing.

In summary, the scaling arguments presented here demonstrate that the extent of the near wake depends not only on the spacing of tip-vortex elements, and thus the tip-speed ratio,
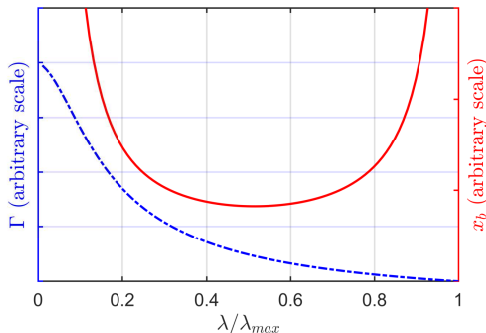
Figure 1: Example plots of the tip-vortex circulation Γ (blue dashed curve, equation 2.8) and tip-vortex breakdown location x_b (red solid curve, equation 2.9) as a function of tip-speed ratio for a parabolic power curve spanning $0 \leqslant \lambda \leqslant \lambda_{max}$ (equation 2.7).

but also on the circulation of the vortices, which is a more complex function of tip-speed ratio and turbine loading.

2.2. *Contributions of turbine thrust to near-wake dynamics*

The arguments in the preceding section highlight the tip-speed ratio as a key parameter for near-wake dynamics. The effects of turbine thrust can be considered within the same scaling framework. Equation 2.1 shows that, for constant tip-speed ratio, increasing C_t will decrease the extent of the near wake. One must also consider 1D momentum theory, which links a higher thrust coefficient to lower flow velocities in the near wake, thus implying that the tip-vortex convection velocity U_c may decrease and potentially lead to further decreases in x_b. Perhaps counterintuitively, this means that a near wake with a low velocity deficit from a low-thrust turbine may persist farther downstream than a higher velocity deficit near wake from a high-thrust turbine. As in the preceding section, these trends are related to tip-vortex circulation as well as tip-vortex spacing.

An additional effect of thrust that the previous arguments do not account for results from the velocity gradients that develop between the wake and free stream. Tip vortices travel at the local flow velocity. Therefore, an outward radial perturbation to a tip vortex will send it towards the free stream and thus into a region of faster-moving fluid, bringing it closer to its unperturbed downstream neighbor. Similarly, an inward radial perturbation will cause a vortex to decelerate and an earlier interaction with its upstream neighbor. Stronger differences between the wake and free-stream velocity will accelerate the time scales of these interactions. Thus, in the presence of radial perturbations, turbine thrust may contribute directly to tip-vortex instability via the near-wake velocity deficit.

The key insight for the purposes of this study is that the mechanisms by which thrust influences the near wake are similar but not identical to the effects of tip-speed ratio. Both parameters impact the streamwise extent of the near wake, but because the thrust coefficient does not always scale directly with tip-speed ratio, the effects of one parameter should not be conflated with the effects of the other. They may augment or interfere with each other, which is a particularly important distinction for time-varying flow conditions.

2.3. *The time-varying character of wind-turbine wakes*

Time-varying dynamics underscore the significance of the preceding theoretical analysis. For steady-flow turbines operating at low tip-speed ratios and thrust coefficients, many of the assumptions commonly made in the literature are warranted. However, even a turbine that conforms precisely to these assumptions in steady flow will display a broader range

of dynamics in time-varying flows as the effects of thrust and tip-speed ratio are further decoupled by the advective nature of the wake.

A time-varying wind-turbine wake is governed by the incompressible Reynolds-averaged Navier-Stokes equations, where we may define a velocity vector u_i that represents a phase average over some periodic oscillation, and a perturbation u_i' that represents turbulent fluctuations occurring at faster time scales than the periodic forcing. The viscous-stress term is neglected due to the high Reynolds numbers. Additionally, pressure recovers rapidly in the near wake and therefore the pressure-gradient term can be neglected after the first couple of turbine diameters (Bempedelis & Steiros 2022). This removes the nonlocal term from the equations, leaving a nonlinear advective partial differential equation of the form

$$\frac{\partial u_i}{\partial t} + u_j \frac{\partial u_i}{\partial x_j} = -\frac{\partial}{\partial x_j} \overline{u_i' u_j'}, \tag{2.10}$$

which admits traveling waves as solutions. Wei *et al.* (2024) have shown that for a quasi one-dimensional flow, this system behaves in a similar manner to the Burgers equation, exhibiting nonlinear wave growth and steepening that is damped by the Reynolds-stress term.

The hyperbolic nature of the governing equations suggests that disturbances at the turbine rotor plane will propagate downstream as traveling waves. Slow or small-amplitude disturbances will advect in a quasi-linear fashion at the local wake velocity, whereas faster or larger-amplitude perturbations may excite nonlinear wave interactions. This is of critical importance for time-varying wind-turbine wakes because it embeds an inherent time delay into the dynamics of the wake. A quasi-steady approximation in which the entire wake immediately adjusts to an upstream disturbance is not possible; the disturbance must propagate in time along the length of the wake.

Taking this view, the advective nature of the turbine wake could decouple the effects of thrust and tip-vortex breakdown on the near and intermediate wake. Changes in thrust would be imparted directly to the flow immediately downstream of the turbine and would then travel downstream at the local streamwise velocity in the wake. Conversely, changes in the tip-vortex circulation and spacing, induced by changes in thrust or tip-speed ratio, would only become apparent at the tip-vortex breakdown location. Thus, we propose that a periodic perturbation in the turbine rotation rate will induce a periodic oscillation in the extent of the near wake, with a time lag dictated by the time it takes for each tip-vortex element to travel to its requisite breakdown location. This time lag would be set by the wake velocity, and thus the oscillations in the near-wake length will be governed not only by the periodic changes in tip-vortex spacing, but also by the thrust variations at the rotor plane. The velocity field in the near wake should then be shaped by thrust and tip-speed ratio variations, and the phase offset between these effects would produce different near- and intermediate-wake configurations.

If this description holds, then careful attention must be paid to both thrust and tip-speed ratio as independent forcing parameters when considering time-varying turbine wakes, with the scaling arguments presented in this section helping to disentangle their respective effects on near and intermediate wake dynamics. Furthermore, if thrust and tip-speed ratio effects can be decoupled as theorized, such a strategy could provide an additional degree of freedom for dynamic wake control strategies to exploit. These theoretical analyses will be explored experimentally in the remainder of this work.

3. Experimental methods

3.1. *Experimental apparatus*

Experiments were conducted in the High Reynolds number Test Facility (HRTF) at Princeton University, which uses pressurized air as the working fluid to obtain Reynolds numbers comparable to those of utility-scale wind turbines while maintaining realistic tip-speed ratios and Mach numbers. The details of the experimental apparatus have been covered in several prior studies (Miller *et al.* 2019; Piqué *et al.* 2022a,b; Kurelek *et al.* 2023; Piqué *et al.* 2024), so only a brief summary is provided here. A schematic of the experiment is shown in figure 2.

All tests in this study were performed at $Re_D = 4 \times 10^6$, using a range of static pressures of up to 170 bar and free-stream velocities between 3.0 and 3.6 ms^{-1} to keep Re_D constant to within $\pm 3\%$. The ambient temperature and pressure in the test section were continuously logged during experiments, and the free-stream velocity was measured using a pitot-static tube located $5.1D$ upstream of the test stand.

A self-starting, three-bladed wind turbine, identical to that employed by Miller *et al.* (2019) except scaled to a rotor diameter of $D = 15$ cm, was used in the experiments. The total blockage when accounting for the rotor swept area and tower was 11%. Aerodynamic forces were measured using a six-axis load cell (JR3 Inc. 30E12A4, 100 N range) at a sampling rate of 1 kHz. Torque and rotation rate were measured using a torque transducer (Magtrol TM-303, 0.5 Nm range) at 200 kHz, from which power was calculated. The load on the turbine was set using a magnetic hysteresis brake (Magtrol AHB-3). Turbine thrust, power, and tip-speed ratio measurements were corrected for blockage using the method of Bahaj *et al.* (2007), and power measurements were also corrected for gearbox losses following Miller *et al.* (2019). Average measurement uncertainties, quantified using the mean standard error over one turbine rotation, were 2.7% for C_t and 0.88% for C_p.

To achieve time-varying perturbations in the wake of the turbine, the braking load applied to the turbine rotor was varied sinusoidally via a reference signal provided to the brake through an amplifier (Kepco BOP72-1.5M). This input waveform was recorded alongside the turbine force and power data for phase synchronization across measurement ensembles.

Measurements of the streamwise flow velocity were obtained in the wake of the turbine by means of a nano-scale thermal anemometry probe (NSTAP) (Bailey *et al.* 2010; Fan *et al.* 2015) and constant-temperature anemometry bridge (Dantec StreamLine Pro) at a sampling rate of 200 kHz. The probe was positioned using a three-axis traverse mounted inside the test section. Two types of measurement sweeps were conducted: (i) streamwise sweeps of 100 logarithmically spaced points along the turbine centerline ($r = 0$) over $1.44 \leqslant x/D \leqslant 10.7$, and (ii) radial sweeps at $x/D = 1.50$, 3.50, and 7.00 over $-1.18 \leqslant r/D \leqslant 1.18$. Calibrations were performed with a reference pitot-static tube before and after each measurement sweep to account for temperature drift in the tunnel. The mean standard error of the phase-averaged velocities was generally between 1.4% and 1.8%, depending on the measurement locations relative to the wake.

3.2. *Design of experiments*

The aim of the experiments is to probe the differing effects of turbine thrust and tip-speed ratio on wake dynamics. To this end, slow time variations in the turbine rotation rate were chosen as a method for forcing the wake in a quasi-steady manner. Forcing the wake at higher frequencies has been shown to excite nonlinear wake dynamics that would obscure the tip-vortex breakdown behaviors of interest to this work (Meyers *et al.* 2022; Messmer *et al.* 2024; Wei *et al.* 2024). Practically, slow time variations also allowed for large-amplitude oscillations in tip-speed ratio, which improved the signal-to-noise ratio of the data while still
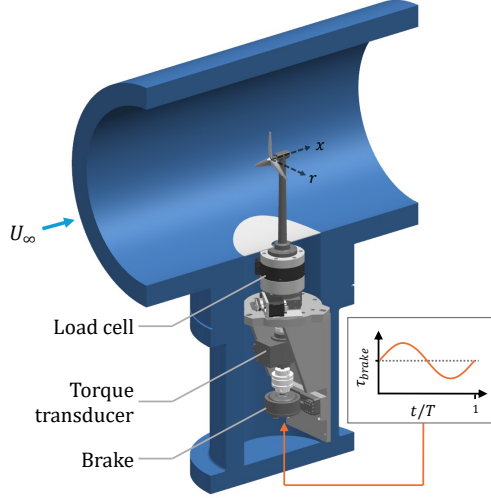
Figure 2: Sectional view of the HRTF test section, including turbine model ($D = 15$ cm) and measurement stack. A sample time-varying torque waveform supplied to the brake is shown in an inset.

avoiding nonlinearities. Thus, for these experiments, the Strouhal number of the tip-speed ratio variations, defined as

$$St = \frac{fD}{U_\infty}, \tag{3.1}$$

was kept in the range $0.02 \leqslant St \leqslant 0.06$ ($0.50 \leqslant f \leqslant 1.52$ Hz with $3.0 \leqslant U_\infty \leqslant 3.6$ ms^{-1} and $D = 15$ cm). This is well below typical values for dynamic induction control, $St \gtrsim 0.2$ (*cf.*, Messmer *et al.* 2024), and therefore is expected to be well within the linear dynamical regime.

Test cases were selected based on the steady-flow thrust and power curves of the turbine, shown in figure 3. The thrust curve has a parabolic shape, with a peak at $\lambda_{\text{opt}} \approx 5$. Therefore, assuming quasi-steady variations along the thrust curve, the local relationship of C_t and λ changes depending on the operating point. For $\lambda < \lambda_{\text{opt}}$, C_t increases with λ. For $\lambda > \lambda_{\text{opt}}$, C_t decreases with increasing λ. This allows the scaling arguments proposed in section 2 for C_t and λ to be tested directly by selecting different mean tip-speed ratios, $\overline{\lambda}$, and imposing variations with peak amplitude $\hat{\lambda}$.

The main experiments presented here involved variations in tip-speed ratio with an amplitude of $\hat{\lambda} = 0.9$ at a Strouhal number of $St = 0.04$. Three mean loading, and therefore steady-flow, conditions were investigated: $\overline{\lambda} = 3.87 \pm 0.07$, 4.89 ± 0.09, and 5.86 ± 0.04. For the time-varying conditions, the brake and turbine gearbox exhibited some hysteresis as a function of changing temperature and pressure conditions in the HRTF. As such, iterative adjustments were made to the mean and peak braking loads prior to each measurement series to ensure $\overline{\lambda}$ and $\hat{\lambda}$ variations remained within predetermined limits of $\overline{\lambda} \pm 0.1$ and $\hat{\lambda} \pm 0.03$. For simplicity, throughout the remaining discussion both the steady and time-varying cases will denoted by $\lambda = \overline{\lambda} + \hat{\lambda}$, with $\hat{\lambda} \approx 0$ assumed for the steady cases, and all other values rounded to one significant digit, thus denoting the time-varying cases as $\overline{\lambda} = 4$, 5 and 6 with $\pm\hat{\lambda} = 0.9$. For completeness, figures will still report the actual values of λ in each test to two decimal places.

For each case, wake measurements were recorded in streamwise and radial sweeps as
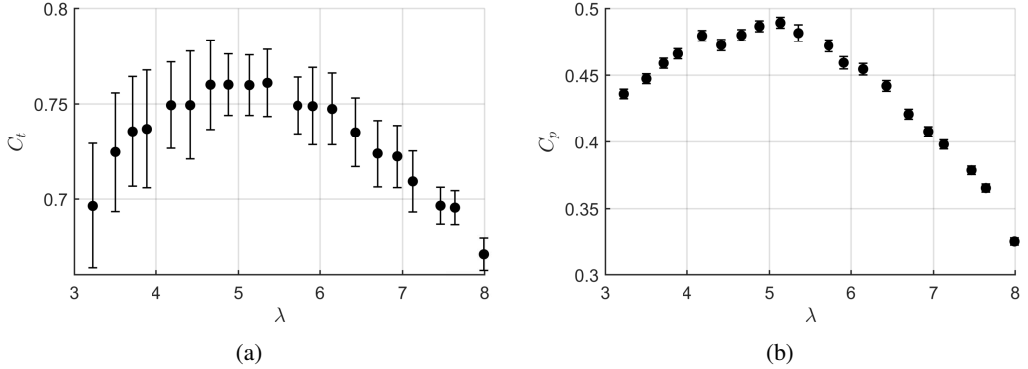
Figure 3: Steady-flow coefficient of thrust (a) and coefficient of power (b).

described in section 3.1. At least 30 full forcing cycles were recorded at each measurement location. The tunnel was allowed to settle for at least 20 minutes between sweeps to allow the temperature to stabilize and thereby ensure accurate calibrations.

Data from time-varying cases were phase-averaged and synchronized based on the phase of the tip-speed ratio waveform. Phase-averaged velocities are denoted by U and time-averaged quantities with an overline, e.g. $\overline{U}$, with the exception of the free-stream velocity U_∞, which is assumed to be constant. The quantity u'^2 represents the streamwise-velocity variance at a given point and phase, taken over the ensemble of cycles used for phase-averaging. The quantity $\overline{u'^2}$ is the time-averaged streamwise-velocity variance.

Finally, two additional forcing frequencies (St = 0.02 and 0.06) and tip-speed ratio amplitudes ($\hat{\lambda}$ = 0.4 and 1.5) were investigated for $\overline{\lambda} \approx 5$. These results are presented in appendices A and B, respectively.

4. Results

4.1. *Steady-flow results*

Steady-flow measurements for $\overline{\lambda} \approx$ 4, 5, and 6 are presented here as a reference for the time-varying cases. The observed trends are similar to those reported by Piqué *et al.* (2024). Velocity and velocity-variance measurements along the wake centerline for the three cases are shown in figure 4. Velocities in the near-wake region ($x/D \lesssim 3$) are similar for all three cases. However, the streamwise extent of the near-wake region is observed to increase monotonically with tip-speed ratio, indicated by the downstream shifts in the location at which the mean velocity profile steepens and where the velocity variance begins to increase, both of which occur within $3 \lesssim x/D \lesssim 4$ in figures 4a and 4b, respectively. These observations are explained by an increased streamwise extent of the helical tip-vortex system, which pushes the point at which the intermediate-wake shear layers converged at the wake centerline further downstream. Furthermore, these trends are consistent with the theoretical description of tip-vortex breakdown given in section 2.1, showing that changes in tip-vortex breakdown cannot be explained by tip-vortex spacing, and thus tip-speed ratio, alone.

Further observations on tip-vortex behavior are made from the radial sweeps of the streamwise velocity variance, shown in figure 5 for three downstream locations. At x/D = 1.50 (figure 5a), the $\overline{\lambda} \approx 6$ case has markedly lower variance peaks due to the tip vortices (at $x/D \approx \pm 0.5$) compared to $\overline{\lambda} \approx$ 4 and 5. These peaks give an indication of the total circulation contained within the tip vortices. Therefore, the assumption that Γ remains constant with $\overline{\lambda}$
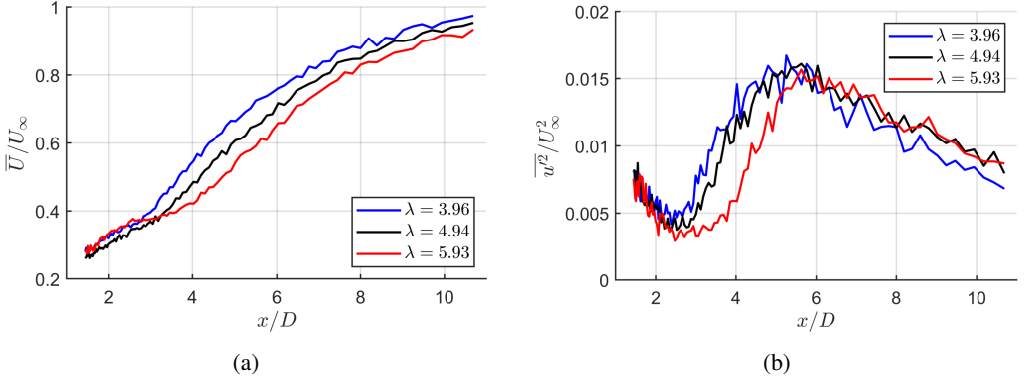
Figure 4: Time-averaged streamwise velocity (a) and velocity variance (b) for three tip-speed ratios in steady flow.
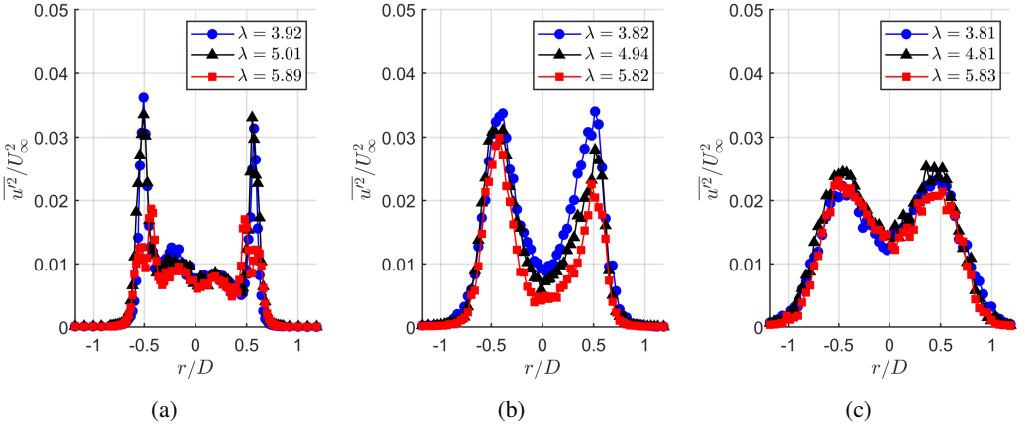

Figure 5: Radial variations in time-averaged streamwise-velocity variance at $x/D = 1.50$ (a), 3.50 (b), and 7.00 (c) at three tip-speed ratios in steady flow.

does not hold for the investigated turbine. This explains the deviation from existing theories for the dependence of tip-vortex breakdown location on tip-speed ratio. The differences in velocity variance as a function of tip-speed ratio are also visible at $x/D = 3.50$ (figure 5b). In the far wake ($x/D = 7.00$, figure 5c), no significant differences are evident as a function of tip-speed ratio. The differences in wake recovery seen in figure 4a suggest that the breakdown of the near wake sets the initial conditions for the development of the far wake. These observations have important implications for both dynamic wake control and actuator-disc modeling efforts. For the former, if the velocity variance in the far wake does not strongly depend on the tip-speed ratio, then the near wake is the critical location for wake-control interventions, as highlighted by recent efforts on controlling near-wake structures (Frederik *et al.* 2020a; Brown *et al.* 2022; van der Hoek *et al.* 2022). For the latter, it is well-established that classic actuator-disc models do not replicate tip-vortex dynamics (Aubrun *et al.* 2013; Lignarolo *et al.* 2014), and therefore require additional modeling efforts to appropriately condition the near wake in the absence of strong free-stream turbulence (Helvig *et al.* 2021; Vinnes *et al.* 2022; Kurelek *et al.* 2023).
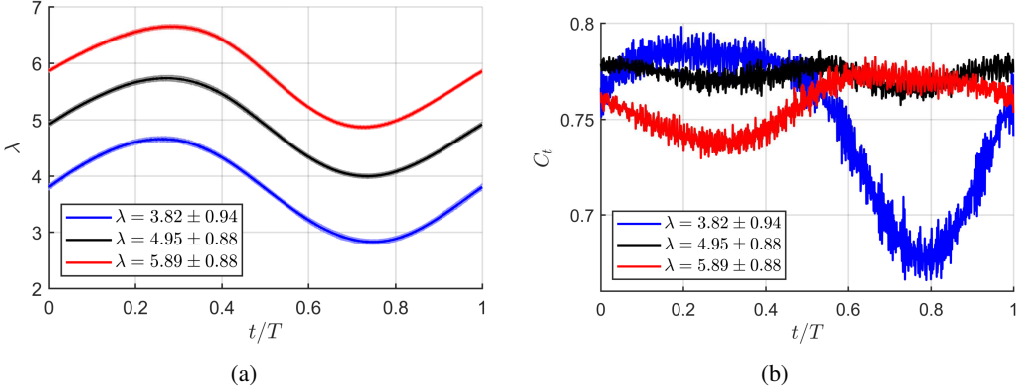
Figure 6: Phase-averaged tip-speed ratio (a) and thrust coefficient (b) for three mean tip-speed ratios. The ± symbol in the plot legends denotes the tip-speed ratio amplitude $\hat{\lambda}$, not an uncertainty. For all cases, $St = 0.04$.

4.2. *Traveling waves in the wake*

Turning now to the time-varying experiments, phase-averaged profiles of tip-speed ratio and thrust coefficient with respect to the intracycle phase, t/T (where $T = 1/f$), are shown in figure 6 for the three tested mean tip-speed ratios. Figure 6b establishes that the variations in C_t are nominally quasi-steady, as across all cases C_t at any particular phase can be recovered from the steady-flow thrust curve (figure 3a) in accordance with the λ value at that phase. For the $\overline{\lambda} \approx 4$ case, C_t increases with λ, and so the phase-averaged thrust coefficient is in phase with the tip-speed ratio oscillation. Conversely, for $\overline{\lambda} \approx 6$, the time-varying C_t profile is out of phase with λ, due to the negative slope of the thrust curve for $\lambda > \lambda_{\text{opt}}$. The $\overline{\lambda} \approx 5$ case shows slight variations, with C_t remaining constant within the measurement uncertainty as the thrust curve is relatively flat at $\lambda = 5$.

In figure 7, the phase-averaged centerline wake velocities are plotted as contours in a space spanned by streamwise distance, x/D, and intracycle phase, t/T. The contour levels present the normalized phase-averaged amplitude of the velocity perturbations, *i.e.*, the phase-averaged velocity $U(x, t)$ with the time-averaged velocity profile $\overline{U}(x)$ subtracted and normalized by the free-stream velocity. These data thus highlight the evolution of velocity perturbations in time and along the wake centerline in the streamwise direction.

Traveling waves are evident in all three cases, seen as red and blue streaks that travel along curved lines in the $x − t$ plane. For $\overline{\lambda} \approx 4$, in which thrust is in phase with tip-speed ratio, the waves are simply advected downstream through the wake (evident in the continuous red and blue swaths in figure 7a). However, for the other two cases, the waves abruptly change sign at $x/D \approx 3$ for $\overline{\lambda} \approx 5$ (figure 7b) and $x/D \approx 3.5$ for $\overline{\lambda} \approx 6$ (figure 7c). As both of these cases stand in contrast to the assumption that C_t scales proportionally with λ (Sørensen *et al.* 2015), this distinctive behavior suggests that thrust and tip-speed ratio are producing competing effects.

Due to the hyperbolic nature of the studied wakes, information must propagate along characteristic curves in $x − t$ space. It is thus beneficial to plot the data in terms of a phase of origin, t_0/T, to highlight the time evolution of fluid parcels as they advect downstream. This is done for each phase-averaged streamwise dataset by forward-Euler integration over the velocity fields. For a fluid parcel at a point (x_k, t_k), the point it would occupy in the next time step is given by (x_{k+1}, t_{k+1}) where $x_{k+1} = x_k + U(x_k, t_k)\Delta t$ and $t_{k+1} = t_k + \Delta t$. By starting at $t_0/T \in [0, 1)$ and $x/D = 1.44$, and interpolating from the phase-averaged velocity
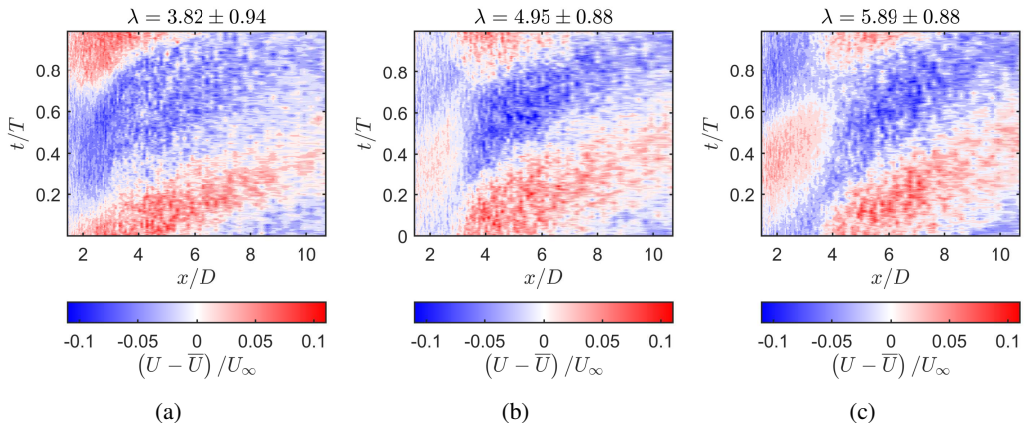
Figure 7: Phase-averaged variations in the streamwise-velocity perturbation, $\left(U - \overline{U}\right)/U_\infty$, along the wake centerline for $\overline{\lambda} \approx 4$ (a), 5 (b), and 6 (c). Note that these and all following contour plots are periodic in time (the vertical axis in this case). For all cases, $\hat{\lambda} \approx 0.9$ and $St = 0.04$.

fields $U(x, t)$ as needed, Lagrangian wake-following contours are constructed in terms of the characteristic variable t_0 and streamwise distance. This process effectively flattens the characteristic curves from figure 7 onto horizontal lines with constant t_0/T, as shown in figure 8. The uniform collapse of the data under this Lagrangian transformation emphasizes the importance of traveling waves for these time-varying wake dynamics.

One final caveat is required before discussing these results further. Because no data were recorded for $x/D < 1.44$, the inception of disturbances from the rotor plane cannot be identified. However, as noted in section 2.3, pressure recovery often occurs in the region of the near wake immediately downstream of the rotor plane. In this region, pressure-gradient forces are significant, and since these forces are nonlocal, thrust information from the turbine is likely communicated nearly instantaneously downstream until the pressure gradient decreases in magnitude. This implies that traveling waves produced by thrust disturbances will appear to begin propagating not from $x/D = 0$ but from farther downstream, where the decreasing influence of pressure-gradient forces allows disturbances to travel at finite speeds.

4.3. *The effects of thrust and tip-vortex breakdown on wake evolution*

The Lagrangian-transformed contours of the velocity perturbation, presented in figure 8, demonstrate the distinct effects of thrust and tip-speed ratio on the time-varying wake dynamics. For $\overline{\lambda} \approx 4$ (figure 8a), the velocity-perturbation waveform aligns with the thrust waveform in figure 6b. Specifically, the velocity perturbation is negative for $0.1 \lesssim t_0/T \lesssim 0.6$, which corresponds with the phase over which the thrust waveform peaks, and the positive velocity-perturbation region matches the phase in which C_t drops below its average value. Uncertainties regarding travel-time phase lags notwithstanding, this matches well with the 1D momentum-theory prediction that higher thrust should correspond to lower near-wake velocities. For $\overline{\lambda} \approx 6$ (figure 8c), the C_t waveform is out of phase with λ, and accordingly the phase of the initial velocity-perturbation waveform in the near wake ($x/D \lesssim 4$) is inverted relative to the $\overline{\lambda} \approx 4$ case. This, however, does not explain the waveform phase inversion that occurs downstream of this region. Additionally, the $\overline{\lambda} \approx 5$ case shows a similar velocity-perturbation wave in the near wake, including a phase inversion at a similar downstream location, despite not having a significant thrust variation. These observations cannot be accounted for by thrust alone.
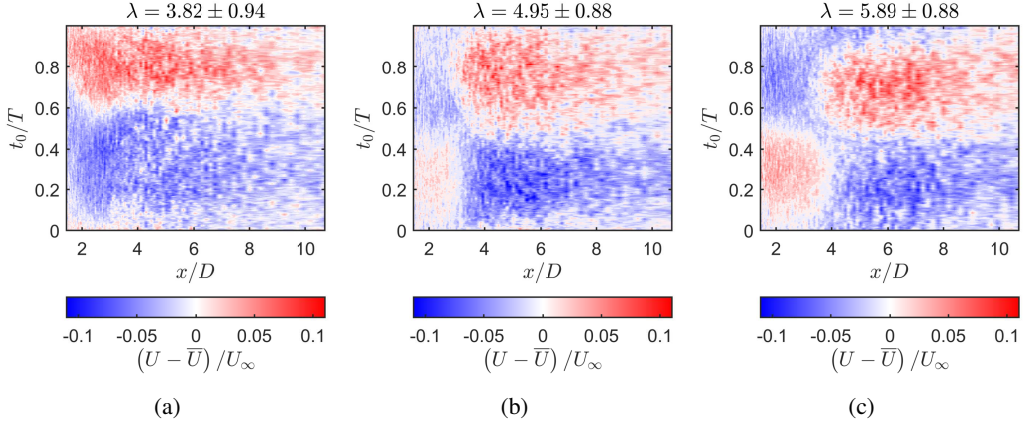
Figure 8: Phase-averaged variations in the streamwise-velocity perturbation along the wake centerline for $\overline{\lambda} \approx 4$ (a), 5 (b), and 6 (c), plotted along characteristics defined by an initial time t_0. For all cases, $\hat{\lambda} \approx 0.9$ and $St = 0.04$.

To demonstrate the cause of these phenomena, Lagrangian-transformed maps of the phase-averaged streamwise velocity U are plotted for the three cases in figure 9. For $\overline{\lambda} \approx 4$, the entire wake shifts back and forth in the streamwise direction – highlighted by considering the highest velocity-deficit region indicated by the blue contours in figure 9a, which recede upstream as the phase advances, creating S-shaped contours. In contrast, the other two cases (figures 9b and 9c) show the intermediate-wake region ($2 \lesssim x/D \lesssim 6$) is deformed by an alternate expansion (for $t_0/T < 0.5$) and compression (for $t_0/T > 0.5$) in the streamwise direction. Such wake deformations can be linked to the phase inversions seen in figures 8b and 8c. The time-averaged velocity profile $\overline{U}$ is not a function of time, and the instantaneous velocity also remains constant in time at the center of the deformed region ($x/D \approx 4$). When the instantaneous velocity profile expands, its slope decreases, and thus the instantaneous velocities upstream of $x/D \approx 4$ will be higher than their corresponding time-averaged values, while the instantaneous velocities downstream of $x/D \approx 4$ will be lower than their corresponding time-averaged values. This will result in a change in sign of the velocity perturbation across this location. When the instantaneous velocity profile is compressed in the following half-cycle, its slope increases, resulting in the opposite effect on the velocity-perturbation profile. The phase inversion of the traveling waves across $x/D \approx 4$ is therefore a consequence of these deformations in the wake profile. Our prior arguments establish this cannot be accounted for by thrust alone, and thus further consideration of the state of the tip-vortex system is warranted.

We argue that the deformations in the intermediate wake result from changes in the tip-vortex breakdown location. Such effects are more readily evident in Lagrangian-transformed contours of the streamwise-velocity variance u'^2, presented in figure 10. In these plots, the near-wake region appears as a dark region with low variance. When the helical tip-vortex system breaks down, the shear layers bounding the wake converge on the centerline, and the velocity variance peaks locally. The tip-vortex breakdown location can thus be visualized by the sharp transition between the dark and light regions. For $\overline{\lambda} \approx 4$ (figure 10a), the tip-vortex breakdown location is farthest upstream when the tip-speed ratio is highest and farthest downstream when λ is lowest, which occurs for $t/T < 0.5$ and $t/T > 0.5$ respectively (cf., figure 6a). These shifts are relatively small since, as evident in the steady-flow variance profiles (figure 4b), the tip-vortex breakdown location does not change appreciably between
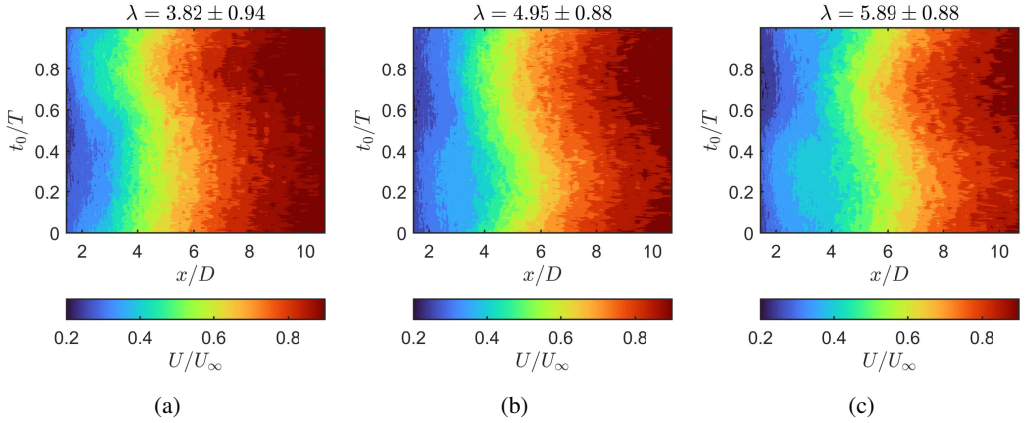
Figure 9: Phase-averaged streamwise velocities along the wake centerline for $\overline{\lambda} \approx 4$ (a), 5 (b), and 6 (c), plotted along characteristics defined by an initial time t_0. For all cases, $\hat{\lambda} \approx 0.9$ and $St = 0.04$.
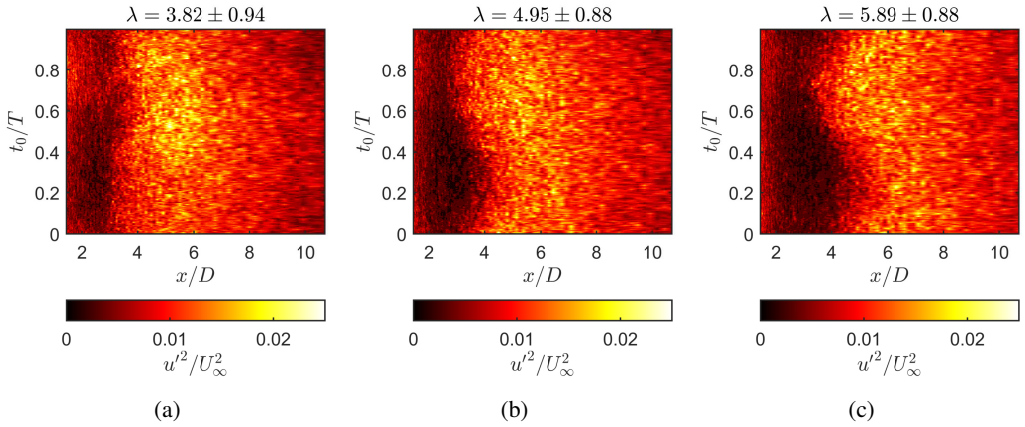

Figure 10: Phase-averaged streamwise-velocity variances along the wake centerline for $\overline{\lambda} \approx 4$ (a), 5 (b), and 6 (c), plotted along characteristics defined by an initial time t_0. For all cases, $\hat{\lambda} \approx 0.9$ and $St = 0.04$.

steady tip-speed ratios of $\overline{\lambda} = 4$ and 5. In contrast, the other two cases show the opposite behavior, with the tip-vortex breakdown location moving downstream when λ is the highest and vice versa. Thus, for these cases, the tip-vortex breakdown location moves in phase with λ, and as with the steady-flow variance plots, the results align well with the scaling arguments from section 2.

Since the tip-vortex breakdown location influences the extent of the near wake, changes in this location will change the geometry of the wake independent of thrust. In the case of $\overline{\lambda} \approx 5$, thrust variations are relatively small and therefore do not significantly affect the near wake, while the shifting tip-vortex breakdown location expands and contracts the intermediate wake, creating oscillations in the wake velocity profile that appear as velocity perturbation waves traveling through the wake. The same dynamics are active in the $\overline{\lambda} \approx 6$ case, but in this case thrust oscillations are larger and therefore are expected to contribute to the expansion and contraction of the near wake. The confluence of the thrust and tip-vortex mechanisms thus affects the topology of the intermediate wake (*e.g.*, compare figures 9b and 9c). In the case of $\overline{\lambda} \approx 4$, it is suspected that the contributions of tip-vortex breakdown dynamics are less evident on the simple basis that variations in thrust amplitude are over twice as large
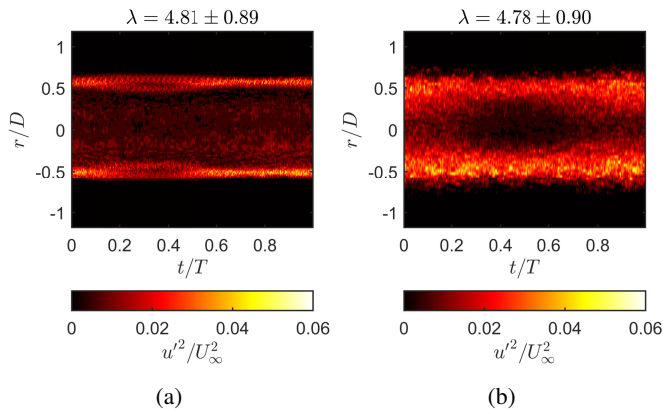
Figure 11: Phase-averaged streamwise-velocity variances along the radial direction at $x/D = 1.50$ (a) and 3.50 (b), both for $\overline{\lambda} \approx 5$. For all cases, $\hat{\lambda} = 0.9$ and $St = 0.04$.

compared to the other cases (figure 6b), resulting in thrust variations dominating over all other dynamics present in the wake.

To observe the tip-vortex dynamics more directly, radial sweeps of the streamwise-velocity variance at two streamwise locations are presented for $\overline{\lambda} \approx 5$ in figure 11. At $x/D = 1.50$ (figure 11a), variations in tip-vortex strength are evident as a function of phase, with stronger tip vortices observed for $t/T > 0.5$ when the tip-speed ratio is lower (*cf*, figure 6a). This aligns with the theoretical predictions for Γ as a function of λ, as discussed in section 2.1 and reported in figure 1. Further downstream at $x/D = 3.50$ (figure 11b), signatures of tip-vortex breakdown and the subsequent convergence of shear layers toward the wake centerline are evident. To determine the advection-based phase lag between these two streamwise locations, we use an empirically fitted linear velocity profile of $U/U_\infty \approx 0.18 + 0.2x/3D$ between $1.5 \leqslant x/D \leqslant 3.5$ and integrate to obtain

$$\frac{t_2 - t_1}{T} \approx 15St \ln\left(\frac{x_2/D + 2.7}{x_1/D + 2.7}\right). \tag{4.1}$$

Thus, the data at $x/D = 3.50$ lag those at $x/D = 1.50$ by $\Delta t/T \approx 0.23$. This means that the weaker tip vortices at $0.2 \lesssim t/T \lesssim 0.5$ in figure 11a can be traced to the larger dark region in figure 11b between $0.4 \lesssim t/T \lesssim 0.7$. Despite being spaced more closely together, the tip vortices in this phase have weaker circulation and therefore extend farther downstream, more effectively shielding the wake from turbulent entrainment and inhibiting wake recovery. Again, these observations align well with the theoretical considerations provided previously. Furthermore, because the thrust variations in this case are negligible, these results lend additional support to the conclusion that tip-vortex breakdown mechanisms are of central importance for near- and intermediate-wake dynamics, and that thrust alone is an insufficient descriptor for the near and intermediate wake.

4.4. *Discussion and implications*

Taken together, these results demonstrate that thrust and tip-vortex breakdown have distinct effects on near- and intermediate-wake dynamics, which can act in complementary or opposing manners to fundamentally alter the shape of the wake velocity profile. This is the case even in slowly time-varying flow conditions. The wake phenomena observed here cannot be reduced to interpolations between steady-flow velocity profiles, and thus cannot be explained using traditional quasi-steady approaches. A consideration of the full dependence

of tip-vortex breakdown on both thrust and tip-speed ratio and a recognition of the advective nature of wake disturbances are both required to reconcile the findings presented in these experiments.

This work has several implications for rotor wakes. The scaling arguments and experimental results show that faster rotor rotation does not guarantee faster tip-vortex breakdown. While this may the case for many wind turbines (*e.g.*, Lignarolo *et al.* 2015; Biswas & Buxton 2024), a more general approach takes the tip-vortex circulation into account, including its dependence on rotor loading. These considerations become more critical for time-varying flows, even those with very slow forcing timescales. Also, while the work has focused on wind-turbine wakes, the fundamental flow physics explored in this study have direct implications for all types of rotor systems in external flows, including hydrokinetic turbines (*e.g.*, Guerra & Hay 2024), helicopter rotors (*e.g.*, Caprace *et al.* 2020), and aircraft and ship propellers (*e.g.*, Di Felice 2004). Any rotor that produces tip vortices and a wake will be subject to the scaling considerations presented in this work. The unsteady nature of flows in the atmospheric boundary layer may make the conclusions of the current study even more relevant for light aerial vehicles such as urban air mobility concepts, small helicopters, and drones (*e.g.*, Mueller & DeLaurier 2003; Jones *et al.* 2022).

From a fluid-mechanics perspective, the findings of this study also provide important context for quasi-steady models of wakes in time-varying flows. In the absence of a pressure gradient, disturbances in these wakes will propagate in an advective manner. As the disturbance moves through the wake, the time history of the disturbance will be distributed spatially along the streamwise extent of the wake. For more complex wake flows with coherent vortex dynamics, such as wind-turbine wakes, advection can alter the topology of the wake in a manner that cannot be reconciled with simple quasi-steady interpolations between steady-flow analogues. We have shown that this is the case even for slow flow variations. For example, for a 100-m diameter wind turbine in a 10-ms^{-1} wind, the Strouhal number of 0.04 used in this study would correspond to a period of 250 seconds – a value well within the range of typical time scales for wind-speed variations in the atmospheric boundary layer (Stull 1988). In a large wind farm, the effects of these types of disturbances will take time to propagate through the array. For a five-turbine array with a spacing of $10D$, this particular disturbance would take at least 8 minutes to reach the last turbine (assuming, very conservatively, that it advects at the mean wind speed). If a wind-farm control scheme uses a quasi-steady flow model that does not account for these advective dynamics, the controller state estimate will be inaccurate and thus will not perform optimally in response to the disturbance. For dynamic wake-control strategies at faster time scales, these considerations are even more important. For time-varying wakes, then, one must be careful when defining and employing a quasi-steady approximation.

Finally, these results have strong implications for dynamic wake control in wind-turbine arrays. Many computational studies on this subject use actuator-disc models with time-varying thrust coefficients (*e.g.*, Goit & Meyers 2015; Munters & Meyers 2017). The present results demonstrate that tip vortices are critical components in time-varying wake dynamics and can shape the velocity profile and recovery characteristics in the near and intermediate wake. This study also serves as a reminder that thrust-coefficient variations are inherently tied to the turbine aerodynamics and therefore cannot always be dictated in an unconstrained manner. In this work, the thrust-coefficient amplitudes were a direct consequence of the thrust curve, and holding the tip-speed ratio amplitude constant meant that the thrust amplitude would vary across cases. Real wind turbines also have inertia and generator dynamics that are often not parameterized in actuator-disc models (El Makdah *et al.* 2021; Wei & Dabiri 2023). This study thus emphasizes the real-world physics that must be taken into account when modeling unsteady wake dynamics for wake-control applications.

It is worth noting that the findings in this study on traveling-wave dynamics and tip-vortex breakdown agree qualitatively with other studies in dynamic wake control conducted at much lower Reynolds numbers, including the recent experiments of Messmer *et al.* (2024) and Wei *et al.* (2024). While to our knowledge no studies have attempted to validate dynamic wake-control strategies in utility-scale flow conditions, the phenomenological agreement observed with previous work does support the idea that dynamic wake control could be just as effective at full scale as it has been in scaled experiments.

5. Conclusions

In this study, the effects of turbine thrust and tip-speed ratio on wind-turbine wake dynamics were investigated by means of theoretical scaling arguments and experiments. The study provides five main contributions to the literature on rotor wakes. First, the theoretical treatment clarifies the relationship of thrust, tip-speed ratio, and tip-vortex breakdown location. In particular, tip-vortex spacing is established as an insufficient indicator for the stability of the vortex system. Second, the experimental apparatus provides a unique method for decoupling the effects of thrust and tip-speed ratio, both in support of the theoretical analysis and as a potential additional control parameter for wind-turbine wake recovery. Third, the measurements demonstrate that wind-turbine wake dynamics behave hyperbolically, in that disturbances propagate downstream along characteristic curves in space and time. This complicates quasi-steady depictions of wake evolution under time-varying conditions. Fourth, the study emphasizes throughout that tip-vortex dynamics are critical for capturing the full dynamics of rotor wakes, particularly for time-varying flows. Finally, the results highlight challenges and opportunities for the modeling and control of wind farms in dynamic flow environments, exposing areas in which more careful modeling efforts are needed, which may unlock new avenues for wind-farm power-density enhancement by independently leveraging both thrust and tip-speed ratio control. Future work will explore dynamic induction control at utility-scale Reynolds numbers and at higher Strouhal numbers than were considered in this study.

Declaration of interests. The authors report no conflict of interest.

Data availability statement. The data that support the findings of this study are available upon reasonable request.

Author ORCID. N. J. Wei, https://orcid.org/0000-0001-5846-6485;
A. Y. Fleisher, https://orcid.org/0009-0001-3034-2904;
J. W. Kurelek, https://orcid.org/0000-0002-8889-3119;
M. N. Hultmark, https://orcid.org/0000-0002-5070-3711

Author contributions. N. J. Wei: Conceptualization, theory, methodology, investigation, analysis, writing – original draft. A. Y. Fleisher: Conceptualization, methodology, investigation, analysis, writing – review & editing. J. W. Kurelek: Conceptualization, methodology, writing – review & editing. M. N. Hultmark: Conceptualization, supervision, writing – review & editing.

Appendix A. Variations in forcing frequency

For the sake of completeness, experimental results in which the forcing frequency and amplitude were varied are included here in appendices.
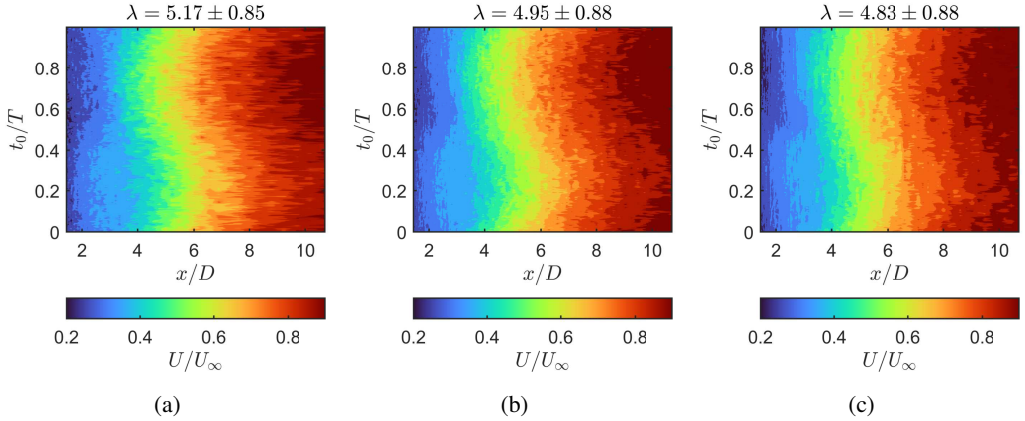
Figure 12: Phase-averaged streamwise velocities along the wake centerline for $\overline{\lambda} \approx 5$ and $St = 0.02$ (a), 0.04 (b), and 0.06 (c), plotted along characteristics defined by an initial time t_0.

Two additional forcing frequencies were tested at $\overline{\lambda} \approx 5$ to demonstrate that the dynamics observed in this study are slow enough as to not depend on frequency. These frequencies corresponded to $St = 0.02$ and 0.06. For the $St = 0.02$ case, data-acquisition limitations meant that 20 periods were included in the phase average for every measurement location. The resulting phase-averaged velocity profiles are shown (along with the previously shown case for $St = 0.04$) in figure 12 in the Lagrangian-transformed characteristic space spanned by t_0/T and x/D (see section 4.2). The velocity profiles appear very similar to each other, demonstrating that there is little variation in the observed dynamics as a function of forcing frequency. This supports the conclusion that $St = 0.04$ is slow enough to count as quasi-steady according to traditional definitions.

Appendix B. Variations in forcing amplitude

Two tip-speed ratio amplitudes, in addition to the case of $\hat{\lambda} \approx 0.9$, were tested to further investigate the differing effects of thrust and tip-speed ratio on the wake. The resulting tip-speed ratio and thrust-coefficient waveforms are shown in figure 13. For both cases, $\overline{\lambda} \approx 5$. The low-amplitude case had no significant thrust variation as a function of time relative to measurement error. The high-amplitude case had an effective oscillation period of half the forcing period, due to the decreases in thrust coefficient on both sides of the thrust peak at $\overline{\lambda} \approx 5$.

Figure 14 shows the phase-averaged velocity-perturbation waves in the wake, plotted in Lagrangian-transformed characteristic coordinates. The dynamics appear qualitatively similar in all cases, highlighting the salience of tip-speed ratio effects over thrust-based effects on the wake. The effect of thrust is to increase the amplitude of the disturbances in the wake, reinforcing the changes in tip-vortex breakdown location that lead to the waveform phase inversion around $x/D \approx 3.5$. For the highest-amplitude case, signatures of the double-peak forcing profile can be seen in the near wake between $2 \lesssim x/D \lesssim 4$, where the switch between positive and negative perturbation values occurs twice within each oscillation cycle. This result emphasizes that both thrust and tip-speed ratio are important factors in dictating near-wake dynamics.

Radial sweeps of the velocity variance are shown for the highest-amplitude case in 15. The radial profiles show similar behaviors to the middle-amplitude case shown in figure 11, including variations in the tip-vortex strength at $x/D = 1.50$ and oscillations in the
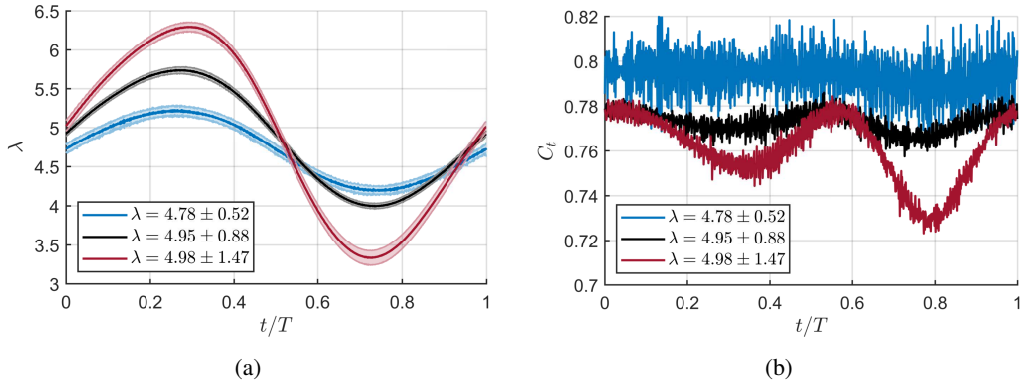
(a)

(b)

Figure 13: Phase-averaged tip-speed ratio (a) and thrust coefficient (b) for three tip-speed ratio amplitudes. For all cases, $\overline{\lambda} \approx 5$ and $St = 0.04$.
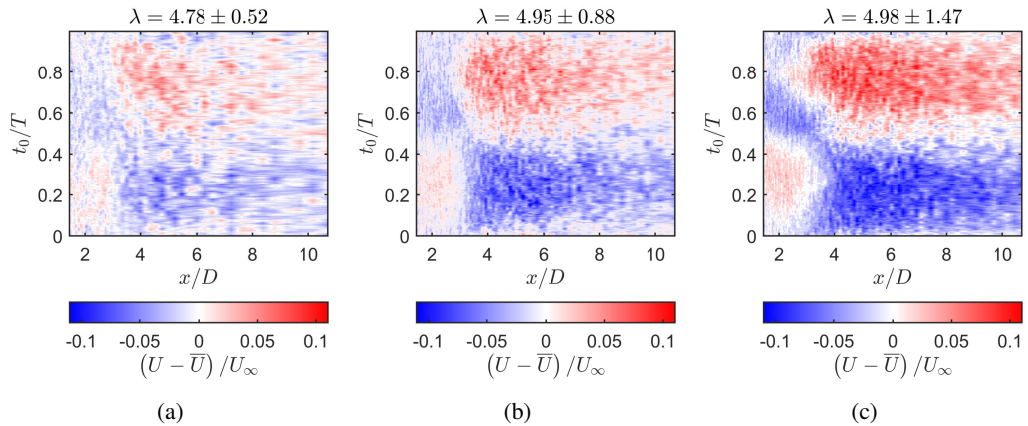

(a)

(b)

(c)

Figure 14: Phase-averaged streamwise velocities along the wake centerline for $\overline{\lambda} \approx 5$ and three different tip-speed ratio amplitudes, plotted along characteristics defined by an initial time t_0.

width of the non-turbulent near-wake region at $x/D = 3.50$. No strong signatures of a half-period forcing are visible in these data. This suggests that, despite the relatively large thrust amplitude, the shifting tip-vortex breakdown location is the primary driver of near- and intermediate-wake dynamics in this case. This case therefore emphasizes that thrust and tip-speed ratio act differently on the wake, particularly in time-varying flow conditions. Thrust alone is insufficient for parameterizing and controlling the wake dynamics. These results also show that manipulating the phase and amplitude relationships between C_t and λ can lead to widely varying classes of wake-velocity profiles.

REFERENCES

AUBRUN, S., LOYER, S., HANCOCK, P.E. & HAYDEN, P. 2013 Wind turbine wake properties: Comparison between a non-rotating simplified wind turbine model and a rotating model. *J. Wind Eng. Ind. Aerodyn.* **120**, 1–8.

BAHAJ, A.S., MOLLAND, A.F., CHAPLIN, J.R. & BATTEN, W.M.J. 2007 Power and thrust measurements of marine current turbines under various hydrodynamic flow conditions in a cavitation tunnel and a towing tank. *Renewable Energy* **32** (3), 407–426.

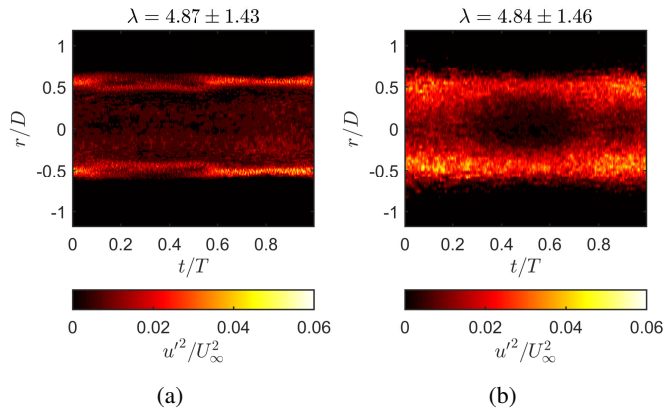BAILEY, SEAN C. C., KUNKEL, GARY J., HULTMARK, MARCUS, VALLIKIVI, MARGIT, HILL, JEFFREY P.,

Figure 15: Phase-averaged streamwise-velocity variances along the radial direction at $x/D = 1.50$ (a) and 3.50 (b), both for $\overline{\lambda} \approx 5$ and $\hat{\lambda} = 1.4$.

MEYER, KARL A., TSAY, CANDICE, ARNOLD, CRAIG B. & SMITS, ALEXANDER J. 2010 Turbulence measurements using a nanoscale thermal anemometry probe. *Journal of Fluid Mechanics* **663**, 160–179.

BARTHELMIE, R. J., HANSEN, K., FRANDSEN, S. T., RATHMANN, O., SCHEPERS, J. G., SCHLEZ, W., PHILLIPS, J., RADOS, K., ZERVOS, A., POLITIS, E. S. & CHAVIAROPOULOS, P. K. 2009 Modelling and measuring flow and wind turbine wakes in large wind farms offshore. *Wind Energy* **12** (5), 431–444.

BARTHELMIE, R. J., PRYOR, S. C., FRANDSEN, S. T., HANSEN, K. S., SCHEPERS, J. G., RADOS, K., SCHLEZ, W., NEUBERT, A., JENSEN, L. E. & NECKELMANN, S. 2010 Quantifying the Impact of Wind Turbine Wakes on Power Output at Offshore Wind Farms. *Journal of Atmospheric and Oceanic Technology* **27** (8), 1302–1317.

BARTL, JAN, MÜHLE, FRANZ, SCHOTTLER, JANNIK, SÆTRAN, LARS, PEINKE, JOACHIM, ADARAMOLA, MUYIWA & HÖLLING, MICHAEL 2018 Wind tunnel experiments on wind turbine wakes in yaw: Effects of inflow turbulence and shear. *Wind Energy Sci.* **3** (1), 329–343.

BASTANKHAH, MAJID & PORTÉ-AGEL, FERNANDO 2014 A new analytical model for wind-turbine wakes. *Renewable Energy* **70**, 116–123.

BEMPEDELIS, N. & STEIROS, K. 2022 Analytical all-induction state model for wind turbine wakes. *Physical Review Fluids* **7** (3), 034605, publisher: American Physical Society.

BISWAS, NEELAKASH & BUXTON, OLIVER R.H. 2024 Effect of tip speed ratio on coherent dynamics in the near wake of a model wind turbine. *Journal of Fluid Mechanics* **979**, A34.

BROWN, KENNETH, HOUCK, DANIEL, MANIACI, DAVID, WESTERGAARD, CARSTEN & KELLEY, CHRISTOPHER 2022 Accelerated Wind-Turbine Wake Recovery Through Actuation of the Tip-Vortex Instability. *AIAA Journal* **60** (5), 3298–3310.

CALAF, MARC, MENEVEAU, CHARLES & MEYERS, JOHAN 2010 Large eddy simulation study of fully developed wind-turbine array boundary layers. *Phys. Fluids* **22** (1), 015110.

CAPRACE, DENIS-GABRIEL, CHATELAIN, PHILIPPE & WINCKELMANS, GRÉGOIRE 2020 Wakes of rotorcraft in advancing flight: A large-eddy simulation study. *Physics of Fluids* **32** (8), 087107.

CERRETELLI, C. & WILLIAMSON, C. H. K. 2003 The physical mechanism for vortex merging. *Journal of Fluid Mechanics* **475**, 41–77.

CHAMORRO, L. P., ARNDT, R. E. A & SOTIROPOULOS, F. 2012 Reynolds number dependence of turbulence statistics in the wake of wind turbines. *Wind Energy* **15** (5), 733–742.

DI FELICE, F. 2004 Experimental Investigation of the Propeller Wake at Different Loading Conditions by Particle Image Velocimetry. *Journal of Ship Research* **48** (02), 168–190.

EL MAKDAH, ADNAN M., ZHANG, KAI & RIVAL, DAVID E. 2021 The scaling of rotor inertia under dynamic inflow conditions. *Journal of Fluids and Structures* **106**, 103357.

FAN, Y., ARWATZ, G., VAN BUREN, T. W., HOFFMAN, D. E. & HULTMARK, M. 2015 Nanoscale sensing devices for turbulence measurements. *Experiments in Fluids* **56** (7), 138.

FELLI, M., CAMUSSI, R. & DI FELICE, F. 2011 Mechanisms of evolution of the propeller wake in the transition and far fields. *Journal of Fluid Mechanics* **682**, 5–53.

FREDERIK, JOERI A., DOEKEMEIJER, BART M., MULDERS, SEBASTIAAN P. & VAN WINGERDEN, JAN-WILLEM 2020*a* The helix approach: Using dynamic individual pitch control to enhance wake mixing in wind farms. *Wind Energy* **23** (8), 1739–1751.

FREDERIK, JOERI ALEXIS, WEBER, ROBIN, CACCIOLA, STEFANO, CAMPAGNOLO, FILIPPO, CROCE, ALESSANDRO, BOTTASSO, CARLO & VAN WINGERDEN, JAN-WILLEM 2020*b* Periodic dynamic induction control of wind farms: proving the potential in simulations and wind tunnel experiments. *Wind Energy Science* **5** (1), 245–257.

GOIT, JAY P. & MEYERS, JOHAN 2015 Optimal control of energy extraction in wind-farm boundary layers. *Journal of Fluid Mechanics* **768**, 5–50.

GUERRA, MARICARMEN & HAY, ALEX E. 2024 Field observations of the wake from a full-scale tidal turbine array. *Renewable Energy* **226**, 120315.

HELVIG, SANNE DE JONG, VINNES, MAGNUS K., SEGALINI, ANTONIO, WORTH, NICHOLAS A. & HEARST, R. JASON 2021 A comparison of lab-scale free rotating wind turbines and actuator disks. *Journal of Wind Engineering and Industrial Aerodynamics* **209** (June 2020), 104485.

VAN DER HOEK, DAAN, VAN DEN ABBEELE, BERT, SIMAO FERREIRA, CARLOS & VAN WINGERDEN, JAN-WILLEM 2024 Maximizing wind farm power output with the helix approach: Experimental validation and wake analysis using tomographic particle image velocimetry. *Wind Energy* **27** (5), 463–482.

VAN DER HOEK, DAAN, FREDERIK, JOERI, HUANG, MING, SCARANO, FULVIO, SIMAO FERREIRA, CARLOS & VAN WINGERDEN, JAN-WILLEM 2022 Experimental analysis of the effect of dynamic induction control on a wind turbine wake. *Wind Energy Science* **7** (3), 1305–1320.

HOWLAND, MICHAEL F., LELE, SANJIVA K. & DABIRI, JOHN O. 2019 Wind farm power optimization through wake steering. *Proceedings of the National Academy of Sciences* **116** (29), 14495–14500.

JONES, ANYA R., CETINER, OKSAN & SMITH, MARILYN J. 2022 Physics and Modeling of Large Flow Disturbances: Discrete Gust Encounters for Modern Air Vehicles. *Annual Review of Fluid Mechanics* **54** (1), 469–493.

KROGSTAD, PER-ÅGE & ADARAMOLA, MUYIWA S. 2012 Performance and near wake measurements of a model horizontal axis wind turbine. *Wind Energy* **15** (5), 743–756.

KURELEK, JOHN W., PIQUÉ, ALEXANDER & HULTMARK, MARCUS 2023 Performance of the porous disk wind turbine model at a high Reynolds number: Solidity distribution and length scales effects. *Journal of Wind Engineering and Industrial Aerodynamics* **237**, 105377.

LEISHMAN, J. GORDON 2002 Challenges in modelling the unsteady aerodynamics of wind turbines. *Wind Energy* **5** (2-3), 85–132.

LIEW, JAIME, HECK, KIRBY S. & HOWLAND, MICHAEL F. 2024 Unified momentum model for rotor aerodynamics across operating regimes. *Nature Communications* **15** (1), 6658.

LIGNAROLO, L.E.M., RAGNI, D., KRISHNASWAMI, C., CHEN, Q., SIMÃO FERREIRA, C.J. & VAN BUSSEL, G.J.W. 2014 Experimental analysis of the wake of a horizontal-axis wind-turbine model. *Renew. Energy* **70**, 31–46.

LIGNAROLO, L. E. M., RAGNI, D., SCARANO, F., SIMÃO FERREIRA, C. J. & VAN BUSSEL, G. J. W. 2015 Tip-vortex instability and turbulent mixing in wind-turbine wakes. *Journal of Fluid Mechanics* **781**, 467–493.

LIMACHER, ERIC J., DING, LIUYANG, PIQUÉ, ALEXANDER, SMITS, ALEXANDER J. & HULTMARK, MARCUS 2022 On the relationship between turbine thrust and near-wake velocity and vorticity. *Journal of Fluid Mechanics* **949**, A24.

MESSMER, THOMAS, HÖLLING, MICHAEL & PEINKE, JOACHIM 2024 Enhanced recovery caused by nonlinear dynamics in the wake of a floating offshore wind turbine. *Journal of Fluid Mechanics* **984**, A66.

MEYERS, JOHAN, BOTTASSO, CARLO, DYKES, KATHERINE, FLEMING, PAUL, GEBRAAD, PIETER, GIEBEL, GREGOR, GÖÇMEN, TUHFE & VAN WINGERDEN, JAN-WILLEM 2022 Wind farm flow control: prospects and challenges. *Wind Energy Science* **7** (6), 2271–2306.

MEYERS, J. & MENEVEAU, C. 2012 Optimal turbine spacing in fully developed wind farm boundary layers. *Wind Energy* **15** (2), 305–317.

MILLER, MARK A., KIEFER, JANIK, WESTERGAARD, CARSTEN, HANSEN, MARTIN O. L. & HULTMARK, MARCUS 2019 Horizontal axis wind turbine testing at high Reynolds numbers. *Physical Review Fluids* **4** (11), 110504.

MUELLER, THOMAS J. & DELAURIER, JAMES D. 2003 Aerodynamics of Small Vehicles. *Annual Review of Fluid Mechanics* **35** (1), 89–111.

MUNTERS, W. & MEYERS, J. 2017 An optimal control framework for dynamic induction control of wind

farms and their interaction with the atmospheric boundary layer. *Philosophical Transactions of the Royal Society A: Mathematical, Physical and Engineering Sciences* **375** (2091), 20160100.

MUNTERS, WIM & MEYERS, JOHAN 2018 Towards practical dynamic induction control of wind farms: analysis of optimally controlled wind-farm boundary layers and sinusoidal induction control of first-row turbines. *Wind Energy Science* **3** (1), 409–425.

OKULOV, V. L. & SØRENSEN, J. N. 2007 Stability of helical tip vortices in a rotor far wake. *Journal of Fluid Mechanics* **576**, 1–25, publisher: Cambridge University Press.

PIQUÉ, A., MILLER, M. A. & HULTMARK, M. 2022*a* Dominant flow features in the wake of a wind turbine at high Reynolds numbers. *Journal of Renewable and Sustainable Energy* **14** (3), 033304.

PIQUÉ, ALEXANDER, MILLER, MARK A. & HULTMARK, MARCUS 2022*b* Laboratory investigation of the near and intermediate wake of a wind turbine at very high Reynolds numbers. *Experiments in Fluids* **63** (6), 106.

PIQUÉ, ALEXANDER, MILLER, MARK A. & HULTMARK, MARCUS 2024 Understanding the effects of rotation on the wake of a wind turbine at high Reynolds number. Version Number: 1.

PORTÉ-AGEL, FERNANDO, BASTANKHAH, MAJID & SHAMSODDIN, SINA 2020 Wind-Turbine and Wind-Farm Flows: A Review. *Boundary-Layer Meteorology* **174** (1), 1–59.

SARMAST, SASAN, DADFAR, REZA, MIKKELSEN, ROBERT F., SCHLATTER, PHILIPP, IVANELL, STEFAN, SØRENSEN, JENS N. & HENNINGSON, DAN S. 2014 Mutual inductance instability of the tip vortices behind a wind turbine. *Journal of Fluid Mechanics* **755**, 705–731.

SEGALINI, ANTONIO & ALFREDSSON, P. HENRIK 2013 A simplified vortex model of propeller and wind-turbine wakes. *Journal of Fluid Mechanics* **725**, 91–116, publisher: Cambridge University Press.

SØRENSEN, JENS N., MIKKELSEN, ROBERT F., HENNINGSON, DAN S., IVANELL, STEFAN, SARMAST, SASAN & ANDERSEN, SØREN J. 2015 Simulation of wind turbine wakes using the actuator line technique. *Philosophical Transactions of the Royal Society A: Mathematical, Physical and Engineering Sciences* **373** (2035), 20140071.

SØRENSEN, JENS N. & VAN KUIK, GIJS A. M. 2011 General momentum theory for wind turbines at low tip speed ratios. *Wind Energy* **14** (7), 821–839.

STEIROS, K. & HULTMARK, M. 2018 Drag on flat plates of arbitrary porosity. *Journal of Fluid Mechanics* **853**, publisher: Cambridge University Press.

STEVENS, RICHARD J.A.M. & MENEVEAU, CHARLES 2017 Flow Structure and Turbulence in Wind Farms. *Annual Review of Fluid Mechanics* **49** (1), 311–339.

STULL, ROLAND B. 1988 *An Introduction to Boundary Layer Meteorology*. Dordrecht: Springer Netherlands.

UBEROI, MAHINDER S. & FREYMUTH, PETER 1970 Turbulent Energy Balance and Spectra of the Axisymmetric Wake. *The Physics of Fluids* **13** (9), 2205–2210.

DE VAAL, J. B., HANSEN, M. O. L. & MOAN, T. 2014 Validation of a vortex ring wake model suited for aeroelastic simulations of floating wind turbines. *Journal of Physics: Conference Series* **555** (1), 012025, publisher: IOP Publishing.

VERMEER, L.J., SØRENSEN, J.N. & CRESPO, A. 2003 Wind turbine wake aerodynamics. *Prog. Aerosp. Sci.* **39** (6-7), 467–510.

VINNES, M. K., GAMBUZZA, S., GANAPATHISUBRAMANI, B. & HEARST, R. J. 2022 The far wake of porous disks and a model wind turbine: Similarities and differences assessed by hot-wire anemometry. *Journal of Renewable and Sustainable Energy* **14** (2), 023304.

WEI, NATHANIEL J. & DABIRI, JOHN O. 2022 Phase-averaged dynamics of a periodically surging wind turbine. *Journal of Renewable and Sustainable Energy* **14** (1), 013305, publisher: American Institute of Physics.

WEI, NATHANIEL J. & DABIRI, JOHN O. 2023 Power-generation enhancements and upstream flow properties of turbines in unsteady inflow conditions. *Journal of Fluid Mechanics* **966**, A30.

WEI, NATHANIEL J., EL MAKDAH, ADNAN, HU, JIACHENG, KAISER, FRIEDER, RIVAL, DAVID E. & DABIRI, JOHN O. 2024 Wake dynamics of wind turbines in unsteady streamwise flow conditions. *Journal of Fluid Mechanics* **1000**, A66.

WIDNALL, SHEILA E. 1972 The stability of a helical vortex filament. *Journal of Fluid Mechanics* **54** (4), 641–663.

ZHANG, WEI, MARKFORT, COREY D. & PORTÉ-AGEL, FERNANDO 2012 Near-wake flow structure downwind of a wind turbine in a turbulent boundary layer. *Exp. Fluids* **52** (5), 1219–1235.